Appl. Phys. B 44, 221–233 (1987)

Applied Physics B Photophysics and Laser Chemistry

Coherent Spectroscopy with a Distributed Feedback Dye Laser

G. M. Gale, P. Ranson*, and M. Denariez-Roberge**

Laboratoire d'Optique Quantique du C.N.R.S., Ecole Polytechnique, F-91128 Palaiseau Cedex, France

Received 15 July 1987/Accepted 22 August 1987

Abstract. A simple and flexible distributed feedback dye laser source pumped by the harmonic of a mode-locked YAG laser is described. Measurements of dephasing times of isotopic and hot bands in CS_2 liquid exploiting both the frequency and time-resolution of this source are reported.

PACS: 42.60, 42.65, 78.30

Nonlinear-optical techniques, with picosecond time resolution, have been applied for some years [1] to the study of vibrational dynamics in condensed matter (liquid or solid). In particular, time-resolved coherent anti-Stokes Raman scattering (CARS) which, in principle at least in its simplest form, provides the same information as spontaneous Raman measurements, can in practice usefully complement this latter technique. Applications have included the determination of vibrational modulation speed in liquids [2], the elimination by time-delayed probing of fast-decaying collision-induced spectral perturbations [3], the investigation of very weak Raman features [3, 4], and the precise determination of the relative vibrational frequencies of the long decay-time components in complex Raman spectra (SEPI [5]). A more recent development [6] exploiting the spatial resolution and nonlocal possibilities of coherent methods, yields information which is practically inaccessible to incoherent spectroscopy.

Nevertheless, time-resolved techniques have suffered from a lack of flexibility in the frequency domain, in that often only a restricted range of vibrational frequencies may be pumped efficiently and the spectral selectivity of such techniques may be much inferior to the Fourier transform limit given by laser temporal behavior. Further, the choice of a source with pulse duration comparable to the shortest relaxation time to be measured may limit application to slower decaying systems, due to decreased excitation through transient effects and (again) inadequate spectral resolution.

Many of the above-mentioned problems would be considerably simplified if a broadly and continuously tunable picosecond domain laser source, being near Fourier transform limited, synchronisable, and having a widely and easily variable pulse duration, were available. In this context, the distributed feedback dye laser, first described by Kogelnik and Shank in 1971 [7] appears capable of fulfilling, at least partially, the stated requirements, and we report here on the performance of such a source, specifically designed for time-domain spectroscopy, and on its application to the measurement of dephasing times in the congested ν_1 vibrational region of the CS_2 molecule, in the pure liquid, and in solution.

1. Description of the Distributed Feedback Source

In the distributed feedback dye laser (DFDL) [8–11] the laser cavity is not formed by external mirrors but is provided by highly frequency-selective Bragg scattering inside the laser medium. This scattering is a result of spatially periodic modulation of the (complex) refractive index of the dye solution. For first-order Bragg scattering the DFDL will oscillate in the vicinity

Present addresses:

* Département de Recherches Physiques, LA 71, Université Pierre et Marie Curie, 4 place Jussieu, F-75252 Paris Cedex 05, France

** LROL Université de Laval, Quebec (Que) G1K 7P4, Canada

of frequency ν_1,

$$\nu_1 = c/(2\eta L), \tag{1}$$

where c is the speed of light in vacuum, η is the mean refractive index of the laser medium and L is the period of the spatial modulation of the refractive index.

For liquid dye lasers, spatial modulation may be provided by pumping the active medium with two interfering laser beams, whose frequency falls in a dye pump band. In this case the modulation of the imaginary part of the refractive index is dominant and a gain grating is formed. Thus both laser gain and laser cavity are provided by the same mechanism of absorption in the dye medium, rendering the device extremely simple. In order to obtain stable operation of the DFDL with low levels of background amplified spontaneous emission, a nearly perfect interference pattern is needed. This requirement is most easily fulfilled, and complex pumping arrangements are avoided, by employing a pump source of high spatial and temporal coherence. For this reason we have chosen to excite our DFDL with the harmonics of a single transverse mode YAG laser which, when mode-locked, also provides pulse durations compatible with our envisaged specifications for system time-resolution. This YAG laser provides a single pulse of 23 ps duration and 10 mJ energy at 532 nm (second harmonic) and a separate pulse of 18 ps length and 0.5 mJ energy at 355 nm (third harmonic) with a repetition rate of 1 Hz. 99.8% of the second-harmonic energy is used to pump an amplifier chain and for coherent vibrational excitation (see below), and the remaining 20 μJ at 532 nm (or 500 μJ at 355 nm) is more than adequate for excitation of all configurations of the DFDL oscillator.

Figure 1 shows a schematic drawing of the oscillator. The 5 mm diameter diffraction-limited pump beam is adjusted in intensity by parallel neutral density filters (F) and is focussed by a spherical or cylindrical lens (L), or by a combination of both, to define the pumping geometry. This beam is then split by the two prisms P1 and P2. Note that in order to have the same focal position for a spherical lens in both the horizontal and vertical planes, these prisms must be set at minimum deviation angle (not shown in Fig. 1). Alternatively, this extra degree of freedom may be exploited in adjusting the pumping geometry. The two resulting beams are directed into the fused quartz dye cell (C) by reflection from two co-rotating mirrors M1 and M2 and two (optional) rotating small-angle prisms P3 and P4.

A fused quartz coupling prism P0 fixed to the dye cell by Canada balsam allows the lasing wavelength λ_l of the DFDL to be less than $\lambda_p \eta$, a limit given by the critical angle of reflection in the absence of P0. The rotation axes of the mirrors M1 M2 are chosen to minimize the relative displacement of the reflected beams at the dye cell when the mirrors are rotated. For mm pumped lengths the configuration shown allows a continuous tuning range of 150 nm without further adjustment. This frequency tuning is achieved by synchronous rotation of either M1 and M2 (fast tuning) or P3 and P4 (slow tuning) by geared-down stepping motors. For our system, tuning rates are

Fast tuning: $\sim 1.3 \times 10^{-1}\,\mathrm{cm}^{-1}$/step

Slow tuning: $(0\text{–}3) \times 10^{-3}\,\mathrm{cm}^{-1}$/step.

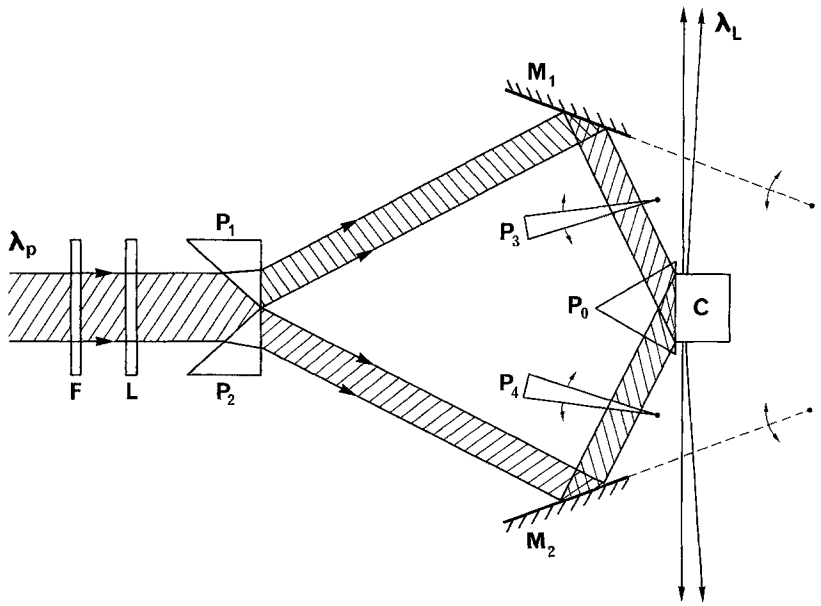

Fig. 1. Schematic drawing of the DFDL oscillator. (F: parallel neutral density filters; L: spherical or cylindrical lens; P_1 and P_2: beam splitting prisms; M_1 and M_2: co-rotating mirrors with axes on the extreme right; P_3 and P_4: co-rotating prisms for fine frequency tuning; P_0: fused quartz coupling prism; C: fused quartz dye cell.) Two equivalent output beams are produced in a direction transverse to the pump beams direction

The wavelength of the DFDL in this configuration is directly proportional to the refractive index of the dye solution η [see (1)]. For alcoholic solvents this leads to a frequency drift of about $7\,\mathrm{cm}^{-1}/°\mathrm{C}$. Rather than try to stabilise dye temperature to better than 1/100 °C we choose to measure this temperature with a platinum thermocouple and to automatically compensate through computer control of the stepping motors. This leads to a dye wavelength absolute stability of less than the laser linewidth over at least the working day and obviates the necessity for continuous measurement of this wavelength.

2. Theory of DFDL

The feedback mechanisms operating in DFDL lasers were first studied by Kogelnik and Shank [8] using a linear analysis based on a coupled-wave model. They assumed a spatial modulation of the real (phase) or imaginary (gain) components of the refractive index of the medium. However, as was noticed by Bor [9] for normal pulsed laser pumping the effect of modulation of the real component of the index is negligible and one need usually only consider gain modulation.

Inside the excited zone L of the dye medium the laser fields may be considered as two counter-propagating waves R and S strongly coupled by Bragg reflection from the gain grating. The laser output intensity I_l, which is proportional to the values of R^2+S^2 at the extremity of the pumped volume, may then be calculated using a set of coupled nonlinear equations describing the dye level populations and the field strengths in time and space [12].

The basic parameters are, for the pumping source

$I_p(t)$: the time-dependent pump rate [photon $\mathrm{cm}^{-1}\,\mathrm{s}^{-1}$]

and for the active medium,

L: the length of the excited region

b: the vertical focus parameter

a: the pumping penetration depth

N: the concentration of dye molecules [cm^{-3}]

σ_a, σ_e: the absorption and emission cross-sections

η: the mean refractive index of the dye solution

τ_f: the lifetime of the excited state

n: the population of the excited state [cm^{-3}]

V: the visibility of the created fringe system.

When the pump duration τ_p is longer than the transit time τ_{tr} of a photon along the excited length L ($\tau_{tr}=\eta L/c$), the spatial variation of the laser field inside the DFDL structure need not be treated in detail. This mean field approximation [9] leads to a set of coupled rate equations whose solution (in good agreement with more elaborate theories [12]) is very useful for practical prediction of the output characteristics of the DFDL as a function of experimental parameters.

These rate equations are, writing q as the average photon density inside the excited volume, and taking into account possible saturation of absorption:

$$dn/dt = I_p\sigma_a(N-n) - \sigma_e cnq/\eta - n/\tau_f, \tag{2}$$

$$dq/dt = \sigma_e cnq/\eta - q/\tau, \tag{3}$$

where τ is the effective cavity lifetime for the photon density q.

$$\tau = \eta L^3(n\sigma_e V)^2/8\pi^2 c \tag{4}$$

and is proportional to the square of the gain coefficient $g(t)$,

$$g(t) = n(t)\sigma_e. \tag{5}$$

One may simplify these equations by introducing the steady state excited population threshold, n_c, obtained by setting $dq/dt=0$ in (3), and the corresponding threshold cavity decay time τ_c,

$$n_c = 2(\pi/V)^{2/3}/\sigma_e L, \tag{6}$$

$$\tau_c = (\eta L/c)/2(\pi/V)^{2/3}, \tag{7}$$

where $(\eta L/c)$ is just the photon transit time τ_{tr}. (For $V=1$, $\tau_c \sim \tau_{tr}/4$). It is also immediately seen that the total required gain at threshold G_c,

$$G_c = \exp(\sigma_e n_c L) = \exp[2(\pi/V)^{2/3}] \tag{8}$$

depends only on fringe visibility V (for $V=1$, $G_c \sim \exp(4)$), and that the amplified spontaneous emission background (a sensitive function of total gain) depends critically on V.

Equation (3) now becomes (writing $\gamma_c = \tau_c^{-1}$),

$$(dq/dt)q^{-1} = \gamma_c[(n/n_c) - (n_c/n)^2] \tag{9}$$

and (2),

$$dn/dt = I_p\sigma_a(N-n) - \gamma_c q(n/n_c) - n/\tau_f \tag{10}$$

with the output power of the DFDL proportional to q/τ.

These coupled nonlinear equations require numerical solution in the general case but some insight into the expected behavior of the DFDL in various situations can be obtained from inspection. Below threshold, one can see from (10) (neglecting for the moment possible saturation of absorption ($n \ll N$) and for pump pulses much shorter than the fluorescence lifetime τ_f) that the excited state population n is simply the integral of the pump pulse,

$$n = \sigma_a N \int_{-\infty}^{t} I_p(t')dt' \qquad n < n_c. \tag{11}$$

Once threshold is reached the DFDL photon density increases at a rate determined by (9). We may define a

Table 1. DFDL photon density exponentiation constants τ_q normalised to cavity transit time τ_{tr} for various levels of excitation n with respect to steady state threshold n_c. Positive values are rise times and negative values fall times

n/n_c	τ_q/τ_{tr}
2	0.13
1.5	0.22
1.2	0.46
1.1	0.85
1.02	4.2
1	∞
0.98	−4.1
0.9	−0.70
0.8	−0.31
0.6	−0.18
0.5	−0.11

(time-dependent) exponential rise-time constant τ_q for q from the right-hand side of this equation

$$\tau_q = \tau_c[(n/n_c) - (n_c/n)^2]^{-1}. \tag{12}$$

Table 1 lists some values of τ_q, normalised to the photon transit time $\tau_{tr} = \eta L/c$, as a function of n/n_c for fringe visibility $V = 1$. One sees that, except when n is very close to n_c, the DFDL photon density rise-times (or fall-times – negative values, Table 1) are near or inferior to the cavity transit time τ_{tr}. This implies that the dynamics of the DFDL are strongly influenced by the length of the pumped region.

3. Short-Pulse Production

If the rates of change of q are faster than pumping rates or, in other words, if $\eta L/c \ll \tau_p$, the DFDL will exhibit self-quenching behavior and q will fall to zero during the pumping pulse. This means that, depending on pumping power the system may be repumped several times and produce more than one pulse. The condition for obtaining a single DFDL pulse, assuming a pump pulse symmetric about $t = 0$, and in the same limits as for (11) may be written approximately,

$$n_c < \Phi < 2n_c : \Phi = \sigma_a N \int_{-\infty}^{\infty} I_p(t')dt' \tag{13}$$

implying stability of single pulse operation against a factor 2 fluctuation in pump intensity (though with considerable jitter of DFDL pulse position inside the pump envelope).

For transit times $\tau_{tr} = \eta L/c$ much less than the pump pulse length τ_p, the pumping will not significantly influence inversion during the DFDL pulse and hence one sees directly from (9, 10, and 12) that, when q is sufficiently small, τ_q will be time-independent, implying near-exponential time-wings for the DFDL pulse. This implicition is bourne out by numerical calculation, as shown in Fig. 2 for a pumped length $L = 600\,\mu$m ($\tau_{tr} = 2.6$ ps), with $\tau_p = 23$ ps and $\Phi = 1.8\,n_c$. In this case the DFDL pulse width at half height $\Delta t_{1/2}$ is ~ 1.6 ps with exponential rise and fall times ~ 0.8 ps and a pulse position jitter of $\sim 25(\Delta\Phi/\Phi)$ ps. Further calculation demonstrates that, for $\tau_{tr} \ll \tau_p$, the DFDL pulse width varies approximately as,

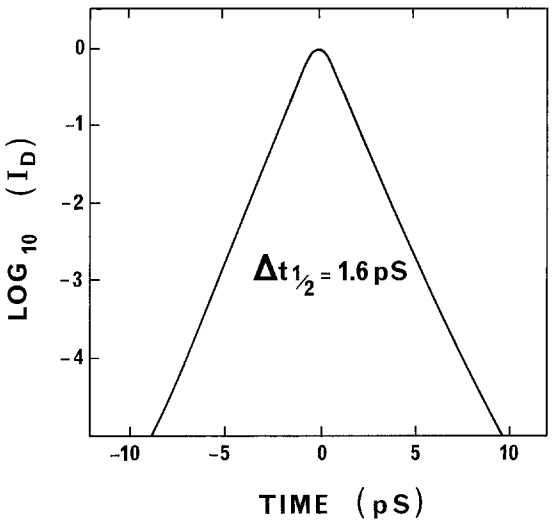

Fig. 2. Calculated DFDL output intensity I_D, plotted on a logarithmic scale versus time in picoseconds for a pumped length $L = 600\,\mu$m and a dye concentration of $2.5 \times 10^{+18}$ mol cm^{-3}. Absorption and emission cross-sections are 4×10^{-16} cm^{-2} and 3×10^{-16} cm^{-2}, respectively. Pump energy is 1.8 times that required to reach steady state threshold as defined by (13), and pump duration is 23 ps. This curve is well described by $I_D = \mathrm{sech}(t/t_A)$ with $t_A = 0.8$ ps here

$$\Delta t_{1/2} \sim (\tau_{tr}\tau_p)^{1/2}/4. \tag{14}$$

However, in practice, $\Delta t_{1/2}$ cannot be decreased indefinitely by reducing the pumped length L, due to factors not included in the calculation. One of these factors is the very large dye concentration required at very small L. From (6) taking $\sigma_e = 1.3 \times 10^{-16}$ cm^2 and $V = 1$ we obtain

$$n_c \sim 3 \times 10^{17}/L(\mathrm{mm})\,[\mathrm{mol\,cm^{-3}}] \tag{15}$$

for the required excited state population. Decreasing L below 100 μm and avoiding saturation ($n \ll N$) gives ground state concentrations in excess of 10^{19} mol cm^{-3} leading to polymerisation, high frequency-dispersion of the refractive index, etc.

In our experimental system, with $\tau_p \sim 20$ ps, the DFDL pulse width is thus limited to $\Delta t_{1/2} > 1$ ps. Figure 3 shows a DFDL pulse autocorrelation mea-

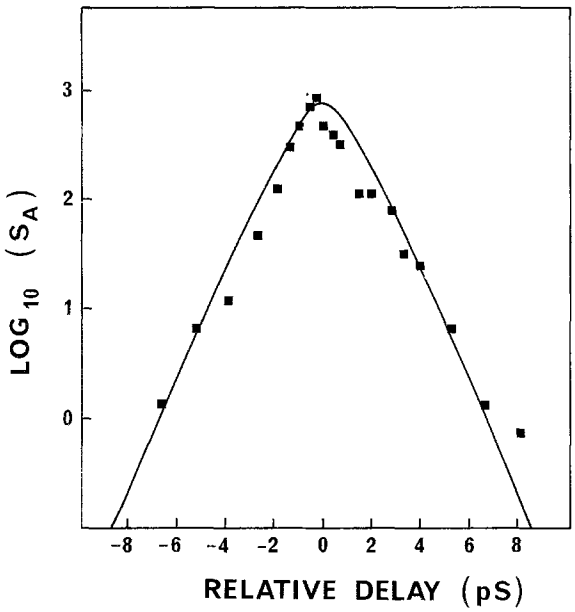

Fig. 3. DFDL autocorrelation function $S_A(t_D) = \int_{-\infty}^{\infty} I_d(t) I_d(t-t_D)dt$, on a logarithmic scale, versus relative delay t_D in picoseconds. Pump energy was ~100 nJ in an 18 ps pulse at 355 nm. The pumped surface was 300 μm long by 30 μm high and dye concentration was 4×10^{18} mol cm^{-3} of Rhodamine 6G. Lasing wavelength was 570 nm. Each experimental point (full squares) represents the average of 20 measurements and hence the figure includes the effects of DFDL pulse-width fluctuations. The full line in the figure is calculated using $I_d = \mathrm{sech}(t/t_A)$ for the DFDL pulse shape and $t_A = 0.75$ ps, leading to a FWHH value of 1.6 ps

surement (obtained by non-collinear sum frequency generation in a KDP crystal) for a pumped length of $L\sim300$ μm in Rhodamine 6G. The pump wavelength was 355 nm. Other parameters are given in the figure caption. Note that each experimental point in Fig. 3 represents the average of 20 shots and hence includes the effects of DFDL pulse width and pump intensity fluctuation. Nevertheless, exponential wings are observed over three orders of magnitude of autocorrelation signal intensity and both the autocorrelation trace and calculated curves in this parameter area are well-described by a sech (t/t_A) pulse shape with, in the illustrated case, $t_A = 0.75$ ps and $\Delta t_{1/2}\sim1.6$ ps.

Spectra of the 1.6 ps average pulse width DFDL, obtained on a shot-by-shot basis, showed a maximum linewidth of 20 cm^{-1} indicating that, for the assumed pulse shape, the Fourier transform limit is exceeded by a maximum of 50%.

Excitation of the DFDL at 532 nm leads to slightly longer pulses ($\Delta t_{1/2} > 2$ ps) due mainly to serious reduction of the pumping penetration depth into the dye cell at this wavelength. Hence diffraction losses limit the usable dye concentration to lower values than at 355 nm.

4. Production of Longer Pulses

The DFDL may also be induced to provide output pulses somewhat longer than the input pump pulse. This is achieved by adjusting two easily accessible parameters; pumped length L and dye concentration N. The effect of the first parameter, operating directly on the photon density time-constant τ_c, has already been discussed. Dye concentration N can play a role in DFDL time-dependence through saturation of absorption.

Decreasing N in (10) to within a few percent of n_c, the steady-state excitation threshold, and correspondingly increasing Φ by changing the pump fluence by several orders of magnitude ($\Phi \gg n_c$), clamps n very close to n_c. This forces the photon density $q(t)$ to closely follow $I_p(t)$, after an initial transient, with

$$q(t)\sim\sigma_a I_p(t)(N-n)\tau_c : n\sim n_c . \tag{16}$$

Clamped excitation is essential for the production of very long unmodulated pulses with $\Delta t_{1/2}\sim\tau_p \gg \eta L/c$ and has been successfully exploited in our system to furnish a pulse of duration $\Delta t_{1/2}\sim1$ ns and spectral width $\Delta\lambda_{1/2} < 7\times10^{-4}$ nm (with nanosecond pump and $L=10$ mm). However, as n_c varies with σ_c^{-1}, (6), clamped excitation limits the "hands-off" tunability range due to the necessity for dye concentration adjustment.

For the production of moderately long pulses $\Delta t_{1/2} \sim \eta L/c$ the role of absorption saturation is much less critical because of the relatively slowed down response of the medium and no limitation to tunability need be imposed. In regard to pumped length L, we find experimentally that $L > c\tau_p/\eta$ leads to increased amplified spontaneous background and accordingly we opted to work at $L = c\tau_p/\eta$ which for excitation at 532 nm (23 ps) gives $L\sim5$ mm. Figure 4 shows the cross-correlation trace of the DFDL pulse $I_D(t)$ with a shorter equivalent gaussian pulse $g(t)$ of FWHH: 15 ps (dashed line in figure)

$$S_{X-COR}(t) = \int_{\infty}^{\infty} I_D(t+\tau)g(\tau)d\tau . \tag{17}$$

As 15 ps is less than the cross correlation trace width, this trace should represent quite well the actual form of $I_D(t)$. We observe a pulse with temporal width ~35 ps which rises rapidly and decays exponentially with a time constant ~12 ps. The corresponding spectral form of this pulse will be discussed in the applications section of this paper. Notice that the cross-correlation measurement extends over six orders or signal magnitude (each point again representing the average of 20 shots) underlining the very clean, background-free nature of the emission from our DFDL laser.

The model we have outlined is not strictly applicable to the above situation for two related reasons. For

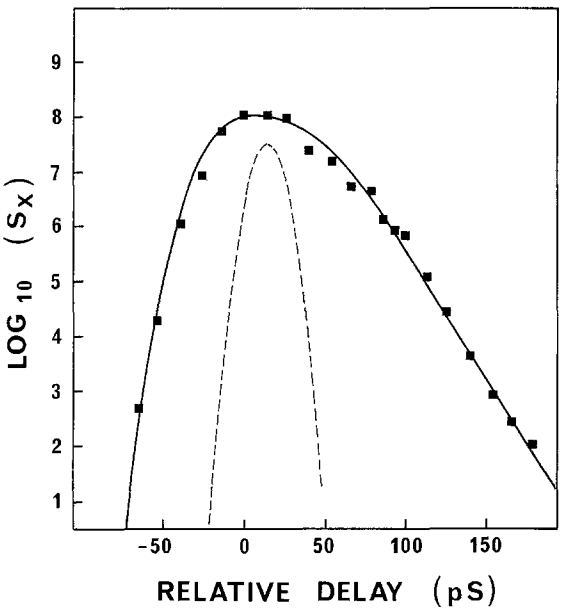

Fig. 4. Cross-correlation between a long DFDL pulse and two 23 ps YAG harmonic pulses, $S_x = \int_{-\infty}^{\infty} I_d(t-t_D)I_y(t)I_y(t)dt$, obtained in a non-resonant time delayed CARS experiment. The cross-correlation signal S_x is plotted on a logarithmic scale versus the relative delay between the DFDL pulse I_d and the two YAG pulses I_y. The shape of the squared YAG harmonic I_y^2 is shown as a dashed line in the figure indicating that the cross-correlation function should be close to the real pulse shape. Pumped length is 5 mm and height is 100 μm with a dye concentration of 8×10^{17} mol cm^{-3} di-sodium fluorescein in ethanol. Pump duration was 23 ps with $\lambda_0 = 551$ nm in this case. The full line in the figure is calculated (see text)

the configuration shown in Fig. 1, although the pumping pulses temporally coincide on the system symmetry axis, as one moves away from this axis by a distance l, a relative time-delay $\sim 2\eta l/c$ is introduced between the two pulses. This means that fringe visibility will significantly decrease at the ends of the pumped region when $\eta L/c$ becomes larger than τ_p. This spatial variation of visibility is not included in the model. The time delay between the two pumping pulses also means that the effective pumping time will increase significantly as one moves away from cell center. Semiempirically we find that we can reproduce the cross-correlation curve of Fig. 4, using (9 and 10), by increasing the effective pump pulse width by approximately a factor of two (that is $\tau_p' \sim \tau_p + \eta L/c$). In these calculations of cross-correlations we must of course also include DFDL pulse position jitter which we find $\sim 20(\Delta\Phi/\Phi)$ ps in this case. The final result (full line in Fig. 4) is in good agreement with the experimental results. This behavior can be understood qualitatively in the following way. The lag of $q(t)$, the DFDL photon density, behind excitation allows n/n_c to achieve relatively large values $n/n_c > 2$ leading to $\tau_q < \tau_{tr}/10$ (Table 1) ($\tau_{tr} \sim 20$ ps here). This produces an initially fast-rising pulse whose subsequent decay is prevented by partial saturation of absorption and damping as n falls through n_c. For the same reasons, as pumping decreases, the system is left with n close to n_c ($n \sim 0.9\, n_c$) and the long-term decay is exponential with a time constant $\sim \tau_{tr}/2$.

We conclude this section on the DFDL laser with a table summarising its properties and parameters in the picosecond and nanosecond pumping regimes (Table 2).

5. Time- and Frequency-Resolved Spectroscopy with the DFDL

5.1 Experimental Set Up and Time Delayed Spectroscopy

One of the applications we envisaged for our DFDL laser system was the possibility of isolating and measuring the coherent relaxation times (T_2) of individual components of complex Raman spectra. In a first experiment we have performed coherent anti-Stokes Raman scattering (CARS) observations of CS_2 liquid

Table 2. Summary of output properties of the DFDL as a function of various parameters including excited length L and pump duration τ_p in the picosecond and nanosecond domain. $N = n_c + \Delta$ indicates that ground state population N is very close to steady state threshold n_c (gain saturation configuration). DFDL energies are quoted after amplification using the set-up of Fig. 5

Pump duration [ps]	3000	23	18
Pump wavelength [nm]	532	532	355
Dye (ethanol soln)	R6G	R6G	R6G
Concentration [N cm^{-3}]	5×10^{16}	2×10^{17}	$> 10^{18}$
Regime	$N = n_c + \Delta$	$N > n_c$	$N \gg n_c$
Pumped length L [mm]	10	5	< 1
DFDL duration [ps]	2000	30	~ 2
Spectral width [cm^{-1}]	3×10^{-2}	0.7	~ 10
Energy [mJ]	2	0.5	~ 0.2
Tunability [nm]	550–590	560–580	570–580

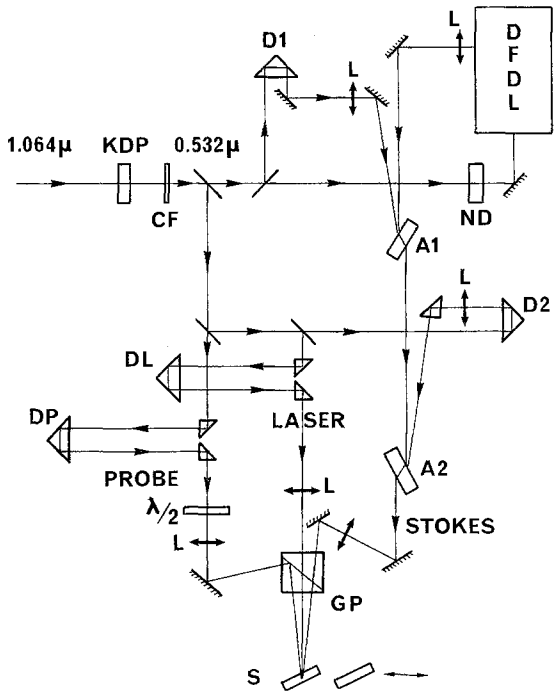

Fig. 5. Schematic outline of the experimental set-up. (DFDL: distributed feedback oscillator. CF: color filter; ND: neutral density filter. A_1, A_2: dye preamplifier and amplifier. D_1, D_2: 532 nm pump delays for A_1 and A_2. $\lambda/2$ half-wave plate; D_p, D_L: probe and laser variable delay lines; L: lens; GP: Glan beam-recombining prism. S: 2 mm thick sample cells)

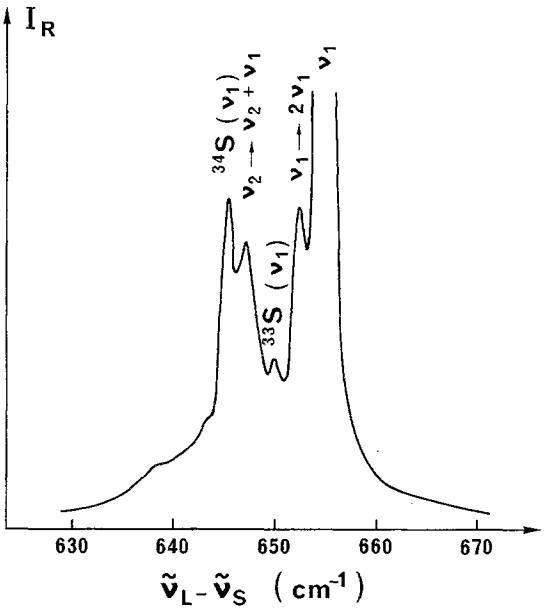

Fig. 6. Spontaneous Raman spectrum of CS_2 liquid in the ν_1 region (redrawn from [14]). Identified in the order of decreasing Raman frequency are the main ν_1 transition, a weak $\nu_1 \rightarrow 2\nu_1$ hot band (1,0; 2,0:32), a weak isotopic transition (0,0; 1,0:33) and the investigated $\nu_2 \rightarrow \nu_1 + \nu_2$ hot band (0,1; 1,1:32) and isotope line (0,0; 1,0:34). A significant broad collision induced background is also seen

in the neighborhood of the ν_1 symmetric stretching vibration. The principal ν_1 line at 656 cm^{-1}, which has a moderately large Raman cross-section, has been extensively investigated by spontaneous Raman spectroscopy [13–16] and time-resolved CARS [17], and its coherent decay-time has been determined as $T_2 \sim 20$ ps. This information enables us to select the time/frequency resolution we require for the experiment.

Figure 5 gives a schematic outline of the experimental setup. The 23 ps, 10 mJ driving pulse at 532 nm is devided into 5 parts, to excite the DFDL oscillator (0.2%), a pre-amplifier (10%), the final amplifier (75%) and to provide pump (10%) and probe (5%) pulses for the coherent Raman experiment. The DFDL oscillator, containing di-sodium fluorescein in ethanol, is excited over $L = 5$ mm to provide a 35 ps long pulse (cross-correlation trace of Fig. 4) tunable around 551 nm. The two amplifier cells containing rhodamine 560 in ethanol transform the weak (1 μJ) divergent (~10 mr) oscillator output into a low divergence (<1 mr), intense (1 mJ) Stokes beam for Raman excitation. Pump and probe beams are suitably time-positioned with respect to the amplified DFDL Stokes beam and are weakly focussed with an 800 mm focal length lens into the 2 mm long sample cell. A non-collinear phase-matching geometry is employed with the probe beam polarised at 90° to the two other beams. The coherent antiStokes signal is detected by a photomultiplier after spatial, polarisation and (adjustable) frequency selection.

Figure 6 shows a Raman spectrum of pure CS_2 liquid, at a temperature of 20 °C, in the region of interest. We employ the notation (v', u'; v'', $u'':I$) to designate a vibrational transition from v' to v'' for ν_1 and from u' to u'' for ν_2. I denotes the mass or masses of isotopic substituents into the parent $^{32}S^{12}C^{32}S$ molecule. The principal features of this quite congested Raman spectrum are identified in the figure caption but it should be noted that, as well as containing relatively narrow isotopic lines and hot bands, this spectrum also exhibits broad and fairly intense collision-induced structure. We are particularly interested in the behavior of the $^{34}S^{12}C^{32}S$ (0,0; 1,0:34) isotopic and the (0,1; 1,1:32) hot bands 10 cm^{-1} below the predominant (0,0; 1,0:32) line, both in the pure liquid and in solution. Although the Raman spectrum shown has insufficient resolution to allow the linewidth of these components to be determined one can already draw some conclusion from the relative intensities. Isotopic abundance (^{34}S, 8%) and temperature (293 K) give estimated integrated intensities of 8% and 30%, respectively, for these lines (normalised to (0,0; 1,0:32). As the Raman spectrum (albeit partially resolved) shows (0,0; 1,0:34) stronger than (0,1;

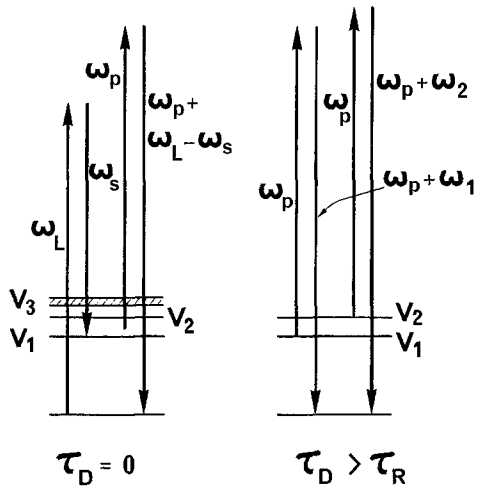

Fig. 7. Difference between ordinary CARS and time-delayed CARS. In ordinary CARS (left of figure) the probe pulse ω_p overlaps in time (delay $\tau_D \cong 0$) with the excitation pulses ω_L and ω_S. The coherent antiStokes signal has a unique frequency $\omega_P + \omega_L - \omega_S$. In time-delayed CARS, for probe delays τ_D greater than the laser pulse widths (τ_R = system response time), broad spectral features corresponding to coherent decays much faster than τ_R will have dissappeared and long decay-time components $\omega_i (T_{2i} > \tau_R)$ give rise to separate anti-Stokes frequencies $\omega_p + \omega_i$. Both these differences can be exploited for efficient isolation of long-T_2 lines in complex Raman spectra

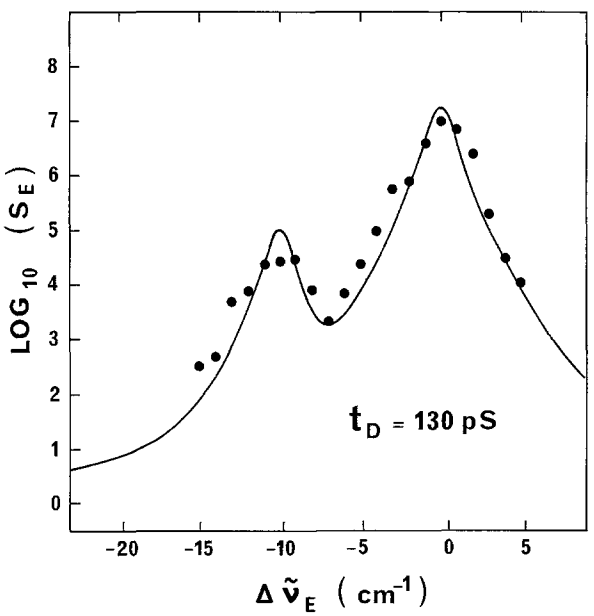

Fig. 8. Time-delayed CARS excitation spectrum of the ν_1 vibrational region of CS_2 liquid. The total observed anti-Stokes signal is plotted on a logarithmic scale versus frequency detuning $\Delta\tilde{\nu}_E = \tilde{\nu}_L - \tilde{\nu}_S - \tilde{\nu}_0$ where $\tilde{\nu}_0$ is the frequency of the principal ν_1 (0,0; 1,0:32) transition. Probe delay t_D was 130 ps and hence only two components of the original Raman spectrum are seen; the principal line at $\Delta\tilde{\nu}_E = 0$ and the next richest isotopic transition (0,0; 1,0:34) at $\Delta\tilde{\nu}_E = -10\,\mathrm{cm}^{-1}$ with 7×10^{-3} of the intensity of the main line. The full line in the figure is calculated (see text)

1,1:32) we conclude that the latter transition must have a significantly larger linewidth than (0,0; 1,0:34) in the pure liquid. This conclusion has immediate consequences for the spectra we observe.

Time resolved CARS frequency spectroscopy differs in two major respects from conventional CARS spectroscopy (Fig. 7). The first difference stems from the fact that delayed probing, at ω_p, of the vibrational coherence allows the elimination of fast-decaying contributions to the Raman spectrum, leading in the frequency-domain to simplified spectra containing only long-T_2 components. The second difference manifests itself when the probe delay is large compared to the duration of excitation at $\omega_L - \omega_S$. In this post-excitation case each species oscillates at its natural frequency ω_i and will thus give rise [18] to different frequencies $\omega_i + \omega_p$ in the antiStokes spectrum. This is in contrast to the conventional CARS situation where all species produce the same antiStokes frequency $\omega_p + \omega_L - \omega_S$ as all oscillators are in forced vibration at $\omega_L - \omega_S$. Both these differences can be exploited in our experiment to provide efficient isolation of selected components of the spectrum.

Figure 8 demonstrates the effect of large probe delay without spectral resolution of the scattered antiStokes signal. In this spectrum the measured signal is plotted on a logarithmic scale versus $\tilde{\nu}_L - \tilde{\nu}_S - \tilde{\nu}_0$, where $\tilde{\nu}_0$ is the frequency of (0,0; 1,0:32), and $\tilde{\nu}_S$ is varied in steps of $1\,\mathrm{cm}^{-1}$ over an interval of $20\,\mathrm{cm}^{-1}$. Probe delay was 130 ps, well outside the range of excitation whose duration is essentially determined by the 23 ps width of the Raman pump pulse ω_L. Only two components of the original complex Raman spectrum remain; the principal line (0,0; 1,0:32) and the next-richest isotope band (0,0; 1,0:34) which appears with 7×10^{-3} of the intensity of the main line. As expected all fast-decaying components, including the (0,1; 1,1:32) hot band, have disappeared, and the (0,0; 1,0:34) isotopic line appears already quite isolated, being, despite its significantly smaller intensity, about 10^4 times larger than the extrapolated wing of the principal (0,0; 1,0:32) line.

Exploiting the second advantage of time-delayed CARS allows even further isolation of the (0,0; 1,0:34) isotopic band. In the excitation spectrum of Fig. 8, taken well after excitation has terminated, the two vibrational components are oscillating at their natural frequencies, differing by $10\,\mathrm{cm}^{-1}$, and the corresponding antiStokes spectrum reflects this difference. Thus, the introduction of spectral resolution of detected radiation can give further discrimination.

Figure 9 illustrates the situation where the detection bandwidth is reduced to $\sim 1\,\mathrm{cm}^{-1}$ centered at $\tilde{\nu}_p + \tilde{\nu}_0 - 10\,\mathrm{cm}^{-1}$. In this case the signal corresponding to the (0,0; 1,0:34) isotope is as large as that of the

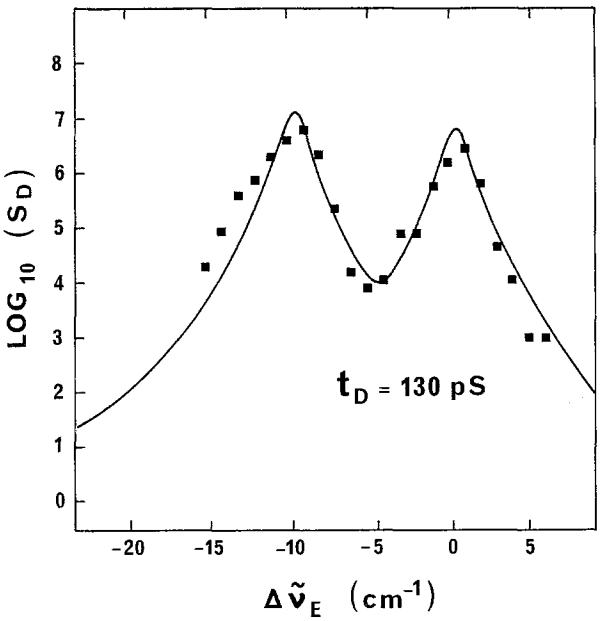

Fig. 9. Time-delayed CARS exictation spectrum in the same conditions as for Fig. 8, except that antiStokes radiation is detected only in a 1 cm^{-1} band centered at the isotope antiStokes frequency $\tilde{\nu}_p+\tilde{\nu}_0-10\,cm^{-1}$. In this case the signal from the isotope is stronger than that from the main line and the isotope is effectively isolated

(0,0; 1,0:32) line in the excitation spectrum and the contamination of this signal may be estimated as $\sim 10^{-6}$. This means that, with excitation centered on the isotope, its coherent evolution can be measured in a time-resolved CARS experiment without risk of perturbation at long times by neighboring lines. Results of this kind will be presented in a subsequent section after a brief discussion of the theory of the spectra shown above.

5.2. Theory

The expected coherent antiStokes signal intensities as a function of DFDL (Stokes) frequency may be calculated in the following way. We suppose initially that only a single component of vibrational frequency ω_0 is present. The coherent vibrational amplitude for off-resonant excitation may be written,

$$Q(t)=k\int_{-\infty}^{t} dt' E_L(t')E_S(t')\exp(i\Delta\omega t')\psi(t-t'), \tag{18}$$

where E_L and E_S are the field envelopes of Raman pump and Stokes beams with frequencies ω_L and ω_s, respectively, and $\Delta\omega=\omega_L-\omega_S-\omega_0$ where ω_0 is the oscillator frequency, which is not included in the coherent amplitude as written here. k is a constant which includes the vibrational line-strength of the transition and $\psi(x)$ is the vibrational relaxation function which in many applications can be approximated as,

$$\psi(x)=\exp(-x/T_2), \tag{19}$$

Probing the coherent amplitude after a time-delay t_D gives a coherent antiStokes signal intensity.

$$S(t_D)=k_2\int_{-\infty}^{\infty} dt|Q(t)E_p(t-t_D)|^2. \tag{20}$$

When probe and excitation fields do not significantly overlap (long-delay probing) the upper limit of integration in (18) can be extended to infinity giving exponentially decaying coherent excitation at long delay,

$$Q(t)=k\exp(-t/T_2)\int_{-\infty}^{\infty} dt E_L(t')E_S(t') \times\exp(t'/T_2)\exp(i\Delta\omega t') \tag{21}$$

or

$$Q(t)\propto\sigma\exp(-t/T_2)R(\Delta\omega,T_2), \tag{22}$$

where σ is the vibration Raman cross-section. The coherent anti-Stokes signal S now has a unique frequency, $\omega_p+\omega_0$.

When several vibrational species of separated frequency ω_i ($\omega_{i+1}-\omega_i\gg T_{2,i}^{-1}+T_{2,i+1}^{-1}$) and Raman cross-section σ_i are involved, in the special case of long delay probing, the total coherent signal intensity is simply the sum of the individual signals at different frequencies

$$S_{tot}(t_D)=\sum_i S_i(t_D,\omega_p+\omega_i), \tag{23}$$

$$S_i(t_D,\omega_p+\omega_i)\alpha\sigma_i^2R^2(\Delta\omega_i,T_{2i})\int_{-\infty}^{\infty} dt \times\exp(-2t/T_{2i})E_p^2(t-t_D), \quad \Delta\omega_i=\omega_L-\omega_S-\omega_i, \tag{24}$$

where the antiStokes frequency $\omega_p+\omega_i$ is indicated for S_i. Note that if probe delay is not large compared with excitation duration, the situation becomes much more complex for multiple vibrational species as the coherent amplitude in (20) will contain a forced component oscillating at $\Delta\omega_i$ and the total signal will have a forced term at $\omega_p+\omega_L-\omega_S$ with contributions, which will interfere, from all species.

In the simple case of long probe delay we may readily calculate the signal employing (21, 24, and 23). We take a Gaussian pulse shape of FWHH: $23/\sqrt{2}$ ps for E_L and E_p and use the computed DFDL pulse shape describe in the section on long pulse production to define E_S. Pump and Stokes relative delay is chosen to optimise the resonant coherent excitation. The result of this calculation, shown in Fig. 8 (full line),

reproduces well the experimental behavior. To take account of the observed relative intensities of the two components of this spectrum (which components have squared relative Raman cross-sections in the ratio 7×10^{-3}) requires a T_2 for the (0,0; 1,0:34) isotopic line close to that for the main (0,0; 1,0:32) transition. This demonstrates that the delayed excitation spectrum already determines quite precisely the dephasing times of its spectral components. Note also that although the wings of the calculated spectrum in Fig. 8 are mainly defined by the rising part of the DFDL pulse and that the fit of the cross-correlation curve of Fig. 4 is most sensitive to the decaying part, the fact that both can be described using the same pulse shape indicates that the real DFDL pulse must be close to Fourier-transform limited.

5.3. *Measurement of Dephasing Times T_2*

Coherent relaxation times are obtained by measuring the variation of the coherent antiStokes signal (20) as a function of probe delay, with fixed excitation frequency and constant bandwidth for the detected antiStokes radiation. When measuring dephasing times of the order of, or shorter, than the pulse durations employed, great care must be exercised to ensure that the system resolution time is adequate and that the observed coherent evolution is in fact resolved. This may be achieved by measuring the system response function which can be obtained most easily in our experiment by replacing the sample cell by an identical cell containing a fluid with no vibrational resonance in the frequency range of interest and maintaining all other parameters fixed. The coherent antiStokes signal S_{NR} generated in this case is due to the 3rd order non-resonant susceptibility of the calibration fluid [1]

$$S_{NR}(t_D)\sim|\chi^{(3)}|^2\int_{-\infty}^{\infty}dt|E_L(t)E_S(t)E_p(t-t_D)|^2 \qquad (25)$$

and gives the system response function as the appropriate cross-correlation function of the three input pulses. In the present experiment cyclohexane is employed as a calibration fluid (and also as a solvent for CS_2).

Figure 10 shows the results obtained for the (0,0; 1,0:34) isotopic line in pure CS_2 liquid at 20 °C (full circles) and for the system response function in pure cyclohexane (full squares). In both cases the DFDL was adjusted to provide resonant excitation of the isotope and the detection bandwidth was $1\,cm^{-1}$ centered at the corresponding antiStokes frequency. The system response function is quite distinct from the isotopic coherent evolution curve in this experiment (being 5 orders of magnitude smaller at a probe delay of 90 ps) and we may consider the upper curve to be well-resolved in the present case. The system response

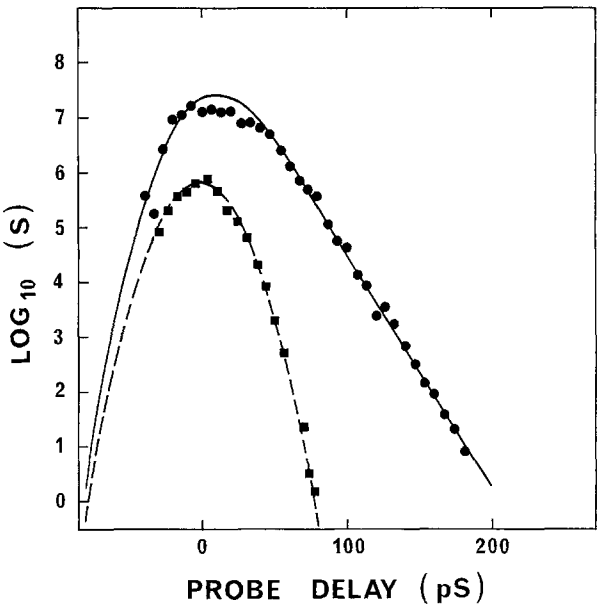

Fig. 10. Coherent antiStokes signal from the (0,0; 1,0:34) isotope line in CS_2 liquid plotted on a logarithmic scale as a function of probe delay in picoseconds (full circles). The DFDL was adjusted to provide resonant excitation of the isotope and the detection bandwidth was $1\,cm^{-1}$ at $\tilde{\nu}_p+\tilde{\nu}_0-10\,cm^{-1}$, the corresponding isotope antiStokes frequency. Also shown (dashed line) is the system time response function. The full line is calculated (see text) yielding a dephasing time of $T_2=21$ ps for the isotope

function may be calculated from (25), using the known pulse shapes, and this calculation reproduces well the experimental points (dashed curve – Fig. 10). Limiting system time-resolution (given by the final slope of the system response function) is <4 ps here, indicating, as expected, that time-resolution is determined especially by the shape of the YAG harmonic pulse and is not significantly degraded by the long (12 ps) exponential tail of the DFDL pulse (Fig. 4).

The coherent evolution of the (0,0; 1,0:34) isotopic line may be calculated using Eqs. (18–20), and the result of this calculation (with $T=21$ ps – full line, Fig. 10) also gives a good account of the observed points, including the time delay of the peak coherent signal with respect to the system response function. The average of several such measurements yields a value of $T_2=21\pm2$ ps for the dephasing time of this isotopic line, We have equally remeasured, in a separate experiment, the coherent decay time of the principal (0,0; 1,0:32) transition and find $T_2=20\pm2$ ps in agreement with previous observations. The significance of these very similar values for dephasing times for the principal and isotopically diluted transitions will be discussed later, but it is already clear that V–V transfer due to long range forces between identical molecules [19] cannot be an important relaxation channel for this mode. The above experimental result

confirms the hypothesis of near-equal T_2 times required to explain the excitation spectra. On the basis of this result one may predict with reasonable confidence that all other isotopic lines (such as (0,0; 1,0:33) will also exhibit very similar dephasing times.

There remains one other important freature in the spectrum of Fig. 6; the (0,1; 1,1:32) hot band which has, as ground state, the thermally populated $v=1$ level of the infrared active v_2 bending vibration. As implied by the Raman spectrum, this transition has a much larger linewidth in the pure liquid than its spectral neighbors. This implication is bourne out by its dissappearance in the delayed CARS spectrum of Fig. 9. However, it has been suggested [15] that this band may narrow considerably when CS_2 is diluted in certain solvents, due to the suppression of a possible broadening channel; that of V–V transfer of v_2, $v=1$ vibrational energy between identical molecules in the pure liquid.

We have accordingly investigated the coherent behavior of weak solutions of CS_2 in the solvent cyclohexane (C_6H_{12}), which solvent we also used to measure the system response function. Our time-resolved CARS spectra show the presence of two additional contributions to the coherent signal in this case. The first contribution is simply due to the solvent cyclohexane. At the low concentrations of CS_2 employed in our experiments (<10%) the non-resonant susceptibility of C_6H_{12} – responsable for the signal we observe when determining the system response function – becomes non-negligible even with respect to the largest Raman cross-section in this spectral region (the (0,0; 1,0:32) line). This contribution may be treated theoretically by adding a term of the form $\chi^{(3)}E_L(t)E_S(t)$ to the coherent vibrational amplitude Q. This term is important only when probe delay is less than ± 50 ps in our present experiment and is furthermore almost frequency independent. The second contribution is centered at $\tilde{\nu}_0 - 8\,\mathrm{cm}^{-1}$ in the excitation spectra (where $\tilde{\nu}_0$ is the vibrational frequency of (0,0; 1,0:32) and is relatively stronger than the (0,0; 1,0:34) isotope line in the pure liquid, at small probe delay, but with a somewhat faster decay (large delay spectra are thus very similar to Fig. 8 taken in the pure liquid).

These spectral data are consistent with the hypothesis of a dilution-slowed hot-band relaxation and may be confirmed by direct measurement of the T_2 of the hot band in solution. To this end we apply the same spectral isolation techniques as for the measurement of the dephasing time of the (0,0; 1,0:34) isotope line in the pure liquid. In the present case the DFDL frequency is adjusted to optimise coherent excitation of the (0,1; 1,1:32) hot-band with respect to the neighboring weaker (0,0; 1,0:34) isotopic line and the detection bandwidth is set to $1\,\mathrm{cm}^{-1}$ at exactly the hot-band

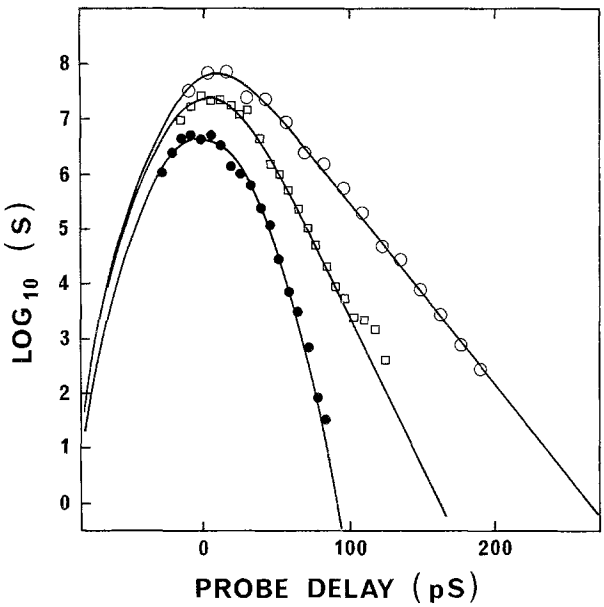

Fig. 11. Coherent antiStokes signals plotted on a logarithmic scale versus probe delay in picoseconds for three different experimental situations: lower curve (full circles); system time-response function obtained using the non-resonant third-order susceptibility of pure cyclohexane, yielding a limiting time resolution ~4 ps. Middle curve (open squares); coherent response of a 5% solution of CS_2 in C_6H_{12} with excitation centered on the (0,1; 1,1:32) hot band and detection set exactly at the hot band antiStokes frequency. The coherent signal is clearly distinct from the system response function at delays greater than 50 ps and gives a coherent decay time $T_2=18$ ps. Upper curve (open circles); coherent signal from the same 5% solution of CS_2 in C_6H_{12} obtained from the principal ν_1 transition (0,0; 1,0:32) yielding a dephasing time of $T_2=26$ ps for this transition. The curves (full lines) are calculated (see text)

antiStokes frequency. The resulting variation of coherent signal with probe delay, for a 5% solution of CS_2 in C_6H_{12} is shown in Fig. 11 (open squares). Also shown are the system response function (full circles) and the behavior of the (0,0; 1,0:32) main line at the same concentration (open circles).

We note first of all that ν_1 decays about 30% more slowly in solution than in the pure liquid, having a $T_2=26$ ps at this concentration (5%). This slight decrease in relaxation efficiency in a lighter, less viscous solvent is in agreement with the general trend predicted by several models [20, 21]. In the light of our measurements in the pure liquid we would expect all other isotopic lines in this spectral region to have essentially the same relaxation time. Our observation of a coherent decay time of 18 ps (Fig. 11 – open squares), significantly different from ν_1 relaxation and system response function, thus confirms that the hot-band (0,1; 1,1:32) at $\tilde{\nu}_0 - 8\,\mathrm{cm}^{-1}$ and the isotopic line (0,0; 1,1:34) at $\tilde{\nu}_0 - 9.5\,\mathrm{cm}^{-1}$ have been successfully

separated in this experiment in solution, despite their close proximity.

We may obtain some further information on the hot-band by theoretically fitting the curves of Fig. 11. As mentioned earlier in this section, in solutions at low concentration of CS_2 in cyclohexane, the non-resonant susceptibility of cyclohexane makes a significant contribution to all coherent signals at small probe delay, and none of the curves in Fig. 11 can be fitted correctly without this non-resonant contribution. This fact allows us to calibrate the relative intensities of the resonance-associated coherent signals irrespective of the absolute signal magnitude, which may vary strongly with other factors, such as alignment. Explicitly we may write, for each isolated vibrational resonance i

$$Q(t) \propto \Gamma \exp(-t/T_{2i}) \int_{-\infty}^{t} dt' E_L(t') E_S(t') \times \exp(i\Delta\omega_i t' + t'/T_{2i}) + E_L(t) E_S(t), \quad (26)$$

where $T_{2i}\Delta\omega_i \ll 1$ here, and

$$S(t_D) = k \int_{-\infty}^{+\infty} dt |Q(t) E_p(t - t_D)|^2 . \quad (27)$$

We suppose the non-resonant susceptibility of cyclohexane independent of frequency over a 10 wavenumber range, and that separation of resonances is perfect. Fitting the constant Γ allows the correct relative signal intensities at small and large probe delays to be obtained. Figure 11 also shows the calculated results obtained in this way with the following sets of (Γ, T_{2i}) parameter pairs (from top to bottom of Fig. 11); (1.0, 26), (0.2, 18) and (0.0, –). We may use these parameter pairs to obtain an estimate of the integrated line-strength I_{HB} of the hot-band relative to ν_1, (0,0; 1,0:32). We find $I_{HB}/I_{\nu_1} = 0.35 \pm 0.05$ which compares favorably with the expected ratio of 0.30 at this temperature [Note that for the (0,0; 1,0:34) isotope this ratio is $I_{iso}/I_{\nu_1} = 0.08$]. This provides further validation of our identification of the (0,1; 1,1:32) hot band as the source of the above observed coherent signal.

5.4. Discussion

We limit our discussion of the measured dephasing times of the symmetric stretching mode of CS_2 to a brief consideration of the basic parameters which control phase relaxation in this case.

For energy-conserving processes, the Raman linewidth Γ of a given transition is determined by the ensemble average of the correlation function of the fluctuations, $\delta\omega$, of the transition frequency [22]

$$\Gamma = \int_{-\infty}^{+\infty} dt \langle \delta\omega(t) \delta\omega(0) \rangle . \quad (28)$$

If V is the interaction potential responsible for these fluctuations we may write, to first order,

$$\delta\omega = \frac{1}{\hbar} \left\{ (V_{aa} - V_{bb}) + \sum_{j \neq i} V_{ij} \right\}, \quad (29)$$

where V_{aa} and V_{bb} are the (time-dependent) matrix elements of the interaction potential between initial states a and between final states b, respectively. V_{ij} denotes formally a vibration-vibration transfer process between the initial molecule i and different molecules j.

For fast-modulation events (homogeneous linewidths) we may rewrite (28) in terms of the correlation time, τ_c, for frequency fluctuations,

$$T_2^{-1} = \langle \delta\omega(0)^2 \rangle \tau_c \quad (30)$$

which shows explicitly the relationship between the inverse dephasing time and the matrix elements of (29), and also demonstrates that the effects of V–V transfer cannot be treated independently of pure frequency-fluctuation broadening.

Our present measurements in pure CS_2 have shown that the dephasing times of the ν_1 mode of $^{32}S^{12}C^{32}S$ (concentration ~91%) and of $^{34}S^{12}C^{32}S$ (concentration ~8%) are identical within experimental error. However, in the latter case, the long-range-force-induced V–V transfer term in (29) is almost fully turned-off, as the excited molecule is almost completely surrounded by non-resonant isotopic molecules. The simplest conclusion is that this long-range V–V term must be negligible with respect to the first term. This conclusion appears reasonable, as the ν_1 mode of $^{32}SC^{32}S$ is infrared inactive thus obviating a common channel of strong V–V transfer via long-range transition–dipole/transition–dipole coupling.

Simple steric arguments show that the effect of V–V transfer via short-range (repulsive) forces should be small (<30%) compared to pure dephasing due to the same repulsive forces [17]. In addition, short-range V–V transfer is very insensitive to isotopic dilution when the energy shift is much smaller than kT [19] which is the case for ν_1 of CS_2. This means that short-range V–V transfer is, in general, indistinguishable from pure dephasing in isotopic dilution experiments and may conveniently be included with it.

The above situation, where long-range V–V transfer makes a negligible contribution to dephasing in the pure liquid, is completely reversed for the (0,1; 1,1:32) hot band. For this band, single quanta of ν_2 vibrational energy can be exchanged between molecules via (long-range) transition-dipole/transition-dipole coupling of the infrared active ν_2 mode, and it is believed that this channel dominates dephasing in the pure liquid [15]. Available Raman spectra do not allow the width of this band to be determined with any precision due to its

proximity to other bands (in particular the (0,0; 1,0:34) isotope line) and the presence of a strong collision induced background. However, the relative intensity of the hot and isotopic bands [15], taking spectral resolution into account, may be used to obtain a lower limit for the hot band width, $\Delta\tilde{\nu}_{HB} > 2\,cm^{-1}$. This lower limit is 4 times larger than the $0.5\,cm^{-1}$ width of the ν_1 fundamental and isotopic satellite.

Dilution of CS_2 in a non-interacting solvent should thus result in a dramatic decrease in the efficiency of this V–V transfer channel leading to T_2 values much greater than the <5 ps estimated above. Our observation of $T_2 = 18$ ps for the hot band in a 5% solution of CS_2 in C_6H_{12} supports this hypothesis. Notice that this value is only slightly smaller than the dephasing time $T_2 = 26$ ps for the fundamental line in the same solution.

Our estimations of matrix elements (29) for the fundamental and hot band in CS_2 lead us to expect very similar dephasing times (within a few percent) for the two transitions in the absence of V–V transfer processes. This result for a *combination* hot band is quite different from that obtained for vibrational *overtones*, where T_2 decreases rapidly with increasing v in the presence of significant anharmonicity. Physically, the difference in the above two processes results from the different effect of *inter-* and *intra*-mode anharmonicity. (For zero anharmonicity the pure dephasing times for all transitions associated with the same mode are identical).

The preceding estimation of near-equal T_2 times for fundamental and hot band in CS_2 is in agreement with the experimental observations and indeed the $\sim 30\%$ shorter T_2 seen for the hot band may readily be attributed to residual V–V transfer between CS_2 molecules in the dilute solution. Nonetheless, further elucidation of this problem will require a systematic study of the dephasing times of fundamental and hot band as a function of CS_2 concentration in various solvents.

6. Conclusion

In conclusion it has been demonstrated that a simple distributed feedback dye laser source can be incorporated into a picosecond CARS experiment, to provide a significant improvement in time and frequency – domain flexibility. The complete system operates close to the theoretical limit for the spectral-selectivity/time-resolution product due to the combination of near-transform – limited tunable DFDL output with gaussian YAG harmonic pulses.

In a first application, the system has been employed to clarify some features of the complex Raman spectrum in the ν_1 region of CS_2 liquid, both pure and in solution. We find, in the absence of long-range V–V transfer, that the dephasing times of all ν_1 transitions (fundamental, isotopic or hot band) are very similar. Further, long-range V–V transfer is identified as a very efficient relaxation channel for the hot band.

We envisage many applications of our experimental system to the investigation of complex or congested Raman spectral features in liquids and solids. In particular, the measurement, analogous to the present work, of isotopic transitions in CO_2 solid should help to elucidate the relaxation mechanisms of the 2-vibron Fermi doublet in this crystal, which has been extensively studied in earlier experiments [23, 24].

Acknowledgements. Two of us (PR and MDR) would like to thank Dr. C. Flytzanis for his invitation to spend a year in the Laboratoire d'Optique Quantique.

References

1. A. Laubereau, W. Kaiser: Rev. Mod. Phys. **50**, 608 (1978)
2. G.M. Gale, P. Guyot-Sionnest, W.Q. Zheng: Optics Commun. **58**, 395 (1986)
3. G.M. Gale, C. Flytzanis, M.L. Geirnaert: In *Phenomena Induced by Intermolecular Interactions*, ed. by G. Birnbaum, NATO ASI Series, Series B: Physics, Vol. 127 (Plenum, New York 1985)
4. M.L. Geirnaert, G.M. Gale: Chem. Phys. **86**, 205 (1984)
5. W. Zinth, H.J. Polland, W. Kaiser: Appl. Phys. B **26**, 77 (1981)
6. G.M. Gale, F. Vallée, C. Flytzanis: Phys. Rev. Lett. **57**, 1867 (1986)
7. H. Kogelnik, C.V. Shank: Appl. Phys. Lett. **18**, 152 (1971)
8. H. Kogelnik, C.V. Shank: J. Appl. Phys. **43**, 2327 (1972)
9. Z. Bor: IEEE QE-**16**, 517 (1980)
10. G. Szabó, Z. Bor, A. Müller: Appl. Phys. B **31**, 1 (1983)
11. T.Sh. Effendiev, W.M. Katarkevich, A.N. Rubinov: Optics Commun. **55**, 347 (1985)
12. Irl N. Duling III, M.G. Raymer: IEEE J. QE-**20**, 1202 (1984)
13. W. Clements, B.P. Stoicheff: Appl. Phys. Lett. **12**, 246 (1968)
14. A.V. Iogansen, B.V. Rassadin, G.I. Romantsova, N.M. Grushina: Opt. Spectrosk. **44**, 1104 (1978) [Opt. Spectros. **44**, 645 (1978)]
15. A.V. Iogansen: Opt. Spectrosk. **45**, 68 (1978) [Opt. Spectrosc. **45**, 36 (1978)]
16. T.I. Cox, M.R. Battaglia, P.A. Madden: Molec. Phys. **38**, 1539 (1979)
17. M.L. Geirnaert: Thèse, Université de Paris-Sud (1984)
18. W. Zinth, H.-J. Polland, A. Laubereau, W. Kaiser: Appl. Phys. B **26**, 77 (1981)
19. J.T. Yardley: *Introduction to Molecular Energy Transfer* (Academic, New York 1980)
20. D.W. Oxtoby: J. Chem. Phys. **70**, 2605 (1979)
21. S.F. Fisher, A. Laubereau: Chem. Phys. Lett. **35**, 6 (1975)
22. R. Kubo: J. Math. Phys. **4**, 174 (1963)
23. G.M. Gale, P. Guyot-Sionnest, W.Q. Zheng, C. Flytzanis: Phys. Rev. Lett. **54**, 823 (1985)
24. P. Ranson, R. Ouillon, S. Califano: J. Raman Spectr. **17**, 155 (1986)